Sci. Rep. Kanazawa Univ. **ARTICLES**
Vol. 68, pp. 83-109, 2025

Electronic structures in magnetic shape memory alloys Fe_3X (X=Pd, Pt) by quasi-particle self-consistent *GW* approach

Artur AKATOV*, Masao OBATA, and Tatsuki ODA

Division of Mathematical and Physical Sciences, Graduate School of Natural Science and Technology, Kanazawa University, Kakuma machi, Kanazawa 920-1192, Japan

(Received December 13, 2024 and accepted in revised form February 21, 2025)

Abstract. By means of a state-of-the-art first-principles calculation of quasi-particle self-consistent *GW* (QSGW) method, we investigated electronic structures and generalized susceptibilities in cubic Fe_3X (X=Pd, Pt) alloys. Compared with those of the density functional method with generalized gradient approximation, the energy band structure indicates both an energy level shift to the high energy side and a narrowing bandwidth in the minority-spin state. Employing the rigid band approximation, the profile of generalized susceptibility was found to indicate the peak positions at $\boldsymbol{q} = (2\pi/a)(1/2,1/2,0)$ for X=Pd and $\boldsymbol{q} = (2\pi/a)(1/8,1/8,0)$ for X=Pt to the modulation wave vector. These modulations may be assigned to the instability of the cubic symmetry phase in the martensitic phase transition observed in the experiment.

Keywords. martensitic transformation, band Jahn-Teller effect, Fermi surface nesting, generalized susceptibility

1 Introduction

Magnetic shape memory alloys have been continuously spotlighted since Ullakko *et al.* [1] found an exotic material of Ni-Mn-Ga alloy: Large magnetic-field-induced strains. Its strain was nearly 0.2% along the [001] direction, although such a ratio was not so large compared with other kinds of shape memory alloys. However, the magnetic materials with shape memory effect have a potential to the application of actuators without imposing external stresses. Nowadays, various kinds of magnetic shape memory alloys are studied in the fields of both basic and applied science along the alloy-suits technological applications such as magneto-mechanical actuators, sensors, and refrigerants [2,3,4]. The series of Ni-Mn-Ga based alloys has still fascinated the researchers and developers who investigate the microscopic/nanoscopic structure of materials [5, 6].

The alloys which have been considered as materials of large magnetic-field-induced strain, apart from the Ni-Mn-Ga based alloys, are in the following: Fe-Pd based, Fe-Pt based, Ni-Mn-Al based, Fe-Ni-Ga based, and Co-Ni-Al based [7,8,9,10]. Although the intensity of studying iron-based Fe-Pd and Fe-Pt tends to be less than Ni-Mn-Ga, the simplicity of structure and large value of magnetic anisotropy, Fe_3Pd and Fe_3Pt are very attractive in understanding behavior of some

* *Corresponding author* E-mail: arturakatov@stu.kanazawa-u.ac.jp

instabilities leading to martensitic transformation. These materials were investigated on martensitic transformation as an invar metal in 1980's [11]. The Fe alloy with 30 atomic % Pd [Fe(100 - x)Pd(x) with x=30] has been well known as good invar, indicating the martensitic transformation from a face centered cubic (FCC) structure to face centered tetragonal (FCT) one at around 270 K [12]. Its transition temperatures near the room temperature provided a long history on research work as well as increased possible applications. One of the important research works on phase transition has been performed in the range of $29.5 < x < 31.5$. In the low concentration range ($29.5 < x < 30.6$), the successive phase transition from the FCT to a body centered tetragonal (BCT) occurs at a decreasing temperature. In the high concentration ($30.6 < x < 31.5$) FCTs have been reported only. For Fe(100 - x)Pt(x), a similar phase diagram has been reported, but its concentration range appears in $25.5 < x < 27.5$ with the low transition temperatures [13]. The number of electrons increases as the x-concentration increases. For example, the case x=30 has 10 more electrons than those of x=25 in Fe(100 - x)X(x).

The electronic structure calculation based on the density functional theory (DFT) has been improved with many qualifications of exchange-correlation functional. Nowadays, the generalized gradient approximation (GGA) is one of the standards, and well-known as a conventional method [14]. Such an approach is powerful for evaluating a lot of kinds of physical quantities. With additional Hubbard U corrections, known as GGA+U, such approaches provide useful tools to sketch the electronic structure of various materials. Using high performance computers, the large size system containing a hundred or thousand atoms in its simulation cell can be applicable to the analysis of electronic structures. Those results obtained allow us to compare with the corresponding experimental counterpart. The GGA+U approaches as well as the GGA are often used for discussions on the comparison with experiment [15,16].

Depending on the quality of physical accuracy and requirement for the comparison, the approaches mentioned in the above paragraph are not sufficient for comparing the experimental results. In particular, the set of energy levels is sometimes obtained as shifted one due to a large electron localization effect in the materials. The band gap of semiconductors is one of typical deviations from the experimental result. For example, the bulk Si has a band gap of about 1 eV in the experiments, while a value reduced to approximately around half is obtained in the GGA calculations [17]. In our experience on the band Jahn-Teller effect in Ni_2MnGa which shows a martensitic transformation, the band to occur on the Fermi level was deviated by about 0.2 eV to the lower energy side in GGA. This energy deviation is not small but rather large when considering the phenomena related to the instability transferring to a low symmetry system at around room temperatures. In the previous work, the theoretical investigation employed a state-of-the-art approach of first-principles electronic structure calculation, quasi-particle self-consistent *GW* (QSGW) method, and found the band of band Jahn-Teller effects to appear just on the Fermi level [18, 19]. Moreover, the analyses of generalized susceptibility found that the Fermi surface nesting occurs at the wave vector which corresponds to the lattice modulation in the low temperature phase. The quality of eigenvalues obtained in the QSGW possibly provides an opportunity to discuss the instability of its martensitic transformation.

The regular alloys, Fe_3X with X=Pd, Pt, have been studied by the approach based on DFT with GGA [20]. The authors investigated the lattice dynamics and structural stability through the calculations of total energies, phonon dispersion relations, Fermi surfaces, etc. The phonon dispersion indicated the instability on the phonon frequency for the transverse acoustic mode at around the wave vector $\boldsymbol{q} = (2\pi/a)(\xi, \xi, 0)$ with $\xi = 1/2$. In addition, the weaker phonon

softening appeared at the wave vectors along the [111] direction. The tendencies of phonon softening were similar between both alloys.

In this work, the electronic structures of the alloys, Fe_3X with X=Pd, Pt, were investigated using the QSGW method, and the instabilities were discussed using the analysis of generalized susceptibility. For X=Pd, the set of eigenvalues for QSGW indicated an energy deviation from those of GGA around the Fermi level and, within the rigid band approximation, the peak position of the generalized susceptibility was obtained at $(2\pi/a)(\xi,\xi,0)$ with $\xi = 1/2$ for the number of electrons (*x*-concentration) at which the martensitic transformation indicates in experiments.

2 Methods and calculation details

The quasi-particle self-consistent *GW* (QSGW) method employs the *GW* approximation (GWA), where the self-energy part of Dyson equation is represented as the product of the one-particle Green's function *G* and the screened Coulomb interaction *W* [21,22]. In QSGW, such a self-energy is used as a set of the exchange-correlation potentials for the inputs of the one particle equation like a Kohn-Sham equation in the DFT approach. The iterative procedure with a self-consistent manner for improving the exchange-correlation potentials provides the band narrowing to localized *d*- or *f*-electron systems. As a consequence, the electron localization effect can be considered in the electronic structure. Electronic states with accurate energy levels appearing on the Fermi level play a critical role in the phenomena, for example, in the phase transition related to band Jahn-Teller effect.

The QSGW method, as well as the method of DFT, the eigenvalues ϵ_j and eigenfunctions $\Psi_j(\boldsymbol{r})$ can be obtained from the following equation:

$$\left[-\frac{\hbar^2}{2m}\nabla^2 + V_{\text{ext}} + V_{\text{H}} + V_{\text{XC}}\right]|\Psi_j\rangle = \epsilon_j|\Psi_j\rangle\,. \tag{1}$$

In this formula, $-\frac{\hbar^2}{2m}\nabla^2$, V_{ext}, V_{H}, V_{XC} are kinetic energy, nuclei, Hartree, exchange-correlation potentials, respectively. In solving ϵ_j and $\Psi_j(\boldsymbol{r})$ with V_{ext} and V_{H}, the V_{XC} is adjusted according to the specific method, QSGW or DFT.

In the QSGW method, the way for obtaining exchange-correlation potential is presented as the following formula:

$$V_{\text{XC}} = \frac{1}{2}\sum_{j,k}|\Psi_j\rangle\left\{\text{Re}\left[\Sigma(\epsilon_j)\right]_{jk} + \text{Re}[\Sigma(\epsilon_k)]_{jk}\right\}\langle\Psi_k|\,, \tag{2}$$

where Re and $\Sigma(\epsilon_j)$ are the Hermitian part and the self-energy, respectively. Self-energy $\Sigma(\epsilon_j)$ can be found from GWA: $\Sigma(\epsilon) = iGW$, where i indicates the imaginary unit. In the practical evaluation, the W is evaluated within random phase approximation as $W = (1 - v\Pi)^{-1}v$, where the polarization function (Π) and the bare Coulomb interaction (v). Once a new set of ϵ_j and $\Psi_j(\boldsymbol{r})$ is obtained, it is used in the evaluations of Π, W, Σ, and V_{XC} for the next iterative cycle. The details of QSGW are referred to the literatures [23, 24].

The regular alloy Fe_3X (X=Pd, Pt) has a structure of $L1_2$ with cubic symmetry. The structure and the 1st Brillouin zone (BZ) are presented in Fig. 1. The lattice constants a for studying are listed in Table I. As seen in Fig. 1(a), three Fe atoms in the unit cell are symmetrically equal and

each Fe has a tetragonal local symmetry. Under cubic symmetry, the five-degenerate d-orbitals are separated into $t_{2g}-$ and e_g-orbitals. The former contains $d_{xy}, d_{yz},$ and d_{zx} orbitals, the latter $d_{x^2-y^2}$ and $d_{3z^2-r^2}$ orbitals. When focusing on the base-centered Fe in xy-plane, t_{2g} is separated into $d_{yz}+d_{zx}$ and d_{xy}, while e_g is separated into $d_{x^2-y^2}$ and $d_{3z^2-r^2}$.

Generalized susceptibility $\chi(\boldsymbol{q})$ can provide the behavior of structural instability. To study the electronic response to modification of the periodic structure is a fundamental reason for calculating this value. The generalized susceptibility determines how strongly electrons of the system respond to disturbance with a wave vector $\boldsymbol{q}$. The main properties of the generalized susceptibility can be related to Fermi surface nesting (FSN). In the present work, the following formula for $\chi(\boldsymbol{q})$ was investigated:

$$\chi(\boldsymbol{q}) = \chi^{\uparrow}(\boldsymbol{q}) + \chi^{\downarrow}(\boldsymbol{q}) = \frac{1}{N_k} \sum_{n,n',\boldsymbol{k},\sigma} \frac{f(\epsilon_{n',\boldsymbol{k}+\boldsymbol{q},\sigma}) - f(\epsilon_{n,\boldsymbol{k},\sigma})}{\epsilon_{n,\boldsymbol{k},\sigma} - \epsilon_{n',\boldsymbol{k}+\boldsymbol{q},\sigma}}, \quad (3)$$

where $\chi^{\uparrow}(\boldsymbol{q})$ and $\chi^{\downarrow}(\boldsymbol{q})$, respectively, denote the majority- and minority-spin contribution, N_k is the number of $\boldsymbol{k}$-points in the 1st BZ, and, $\epsilon_{n,\boldsymbol{k},\sigma}$ and f are the eigenvalues and Fermi distribution function, respectively, for the states specified with the band index n, wave vector $\boldsymbol{k}$, and spin index σ. The function f is parametrized with the Fermi energy ϵ_{F}.

The large value of the $\chi(\boldsymbol{q})$ for wave vector $\boldsymbol{q} = (2\pi/a)(\xi_x, \xi_y, \xi_z)$ can indicate strong FSN effect. This means that the wave vector $\boldsymbol{q}$ corresponds to the direction along which the Fermi surfaces are efficiently nested. Such a type of amplification, when the electron-phonon interaction is not reduced sufficiently, may indicate structural and electronic instability of the system, which predicts structural phase transition to modulated structures or new type of symmetry. In this work, to investigate the feature of the x-concentration dependence, the analysis of the rigid band approximation to $\chi(\boldsymbol{q})$ was applied. This approximation can predict an x-concentration dependence for Fe(100-x)X(x).

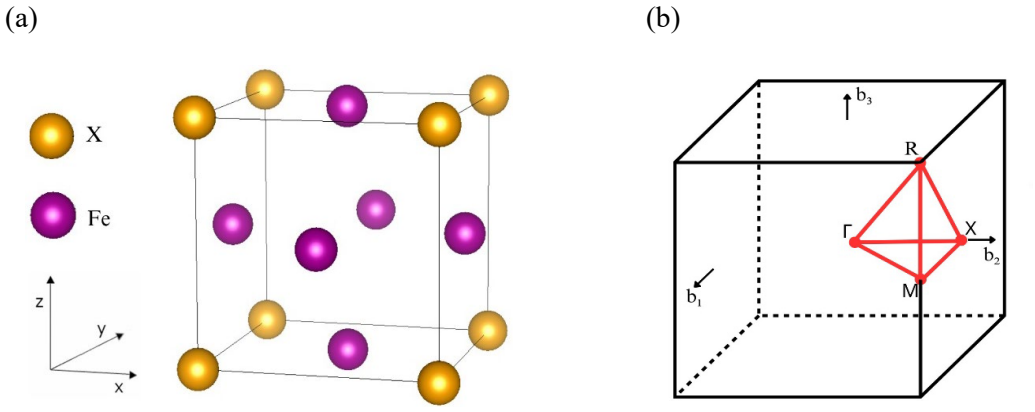

Fig. 1. (a) Unit cell for cubic Fe_3X (X=Pd, Pt) structure; (b) 1st Brillouin zone (BZ) with symmetric points and paths for band dispersion curve.

Table I. Lattice constants (a) of the $L1_2$ structure Fe_3X (X=Pd, Pt).

	Fe_3Pd	Fe_3Pt
Lattice constant [Å]	3.79 [25]	3.73 [26]

For both QGSW and GGA calculation, the same grid points of $10 \times 10 \times 10$ mesh in 1st BZ were used for the self-consistent calculation. This amounts to 56 points of $\boldsymbol{q}$ wave vector for the most time-consuming part of polarization function Π in each iterative self-energy cycle. The DFT method employed GGA of the Perdew-Burke-Ernzerhof (PBE) exchange and correlation potential [27]. The computations of QSGW and GGA were carried out using the implementation of *ecalj* package [28]. For the QSGW calculations of Fe_3Pd and Fe_3Pt, we employed a mixed basis set combining highly localized muffin-tin orbitals (MTOs) and Augmented Plane-Wave (APW). The plane-wave cutoff energy was set to 3 Ry, optimized to balance accuracy and computational efficiency. The muffin-tin radii were chosen as R_{MT} = 2.46 bohr for both Pd and Fe atoms in Fe_3 Pd structure, and R_{MT} = 2.47 bohr for Pt and R_{MT} = 2.36 bohr for Fe in Fe_3Pt structure. The k-point mesh used for the density of states (DOS) calculations was $10 \times 10 \times 10$ in the 1st Brillouin zone for both structures. The convergence criteria were set to 10 meV for the maximum change in all calculated quasi-particle energies. This means that the iterative process will be carried out until the maximum energy difference between successive iterations becomes lower than this value. In the $\chi(\boldsymbol{q})$ calculation, the grid points of $80 \times 80 \times 80$ mesh were used in the 1st BZ. In addition, for the calculation of Fe_3Pt, effects of spin-orbit interaction (SOI) were investigated because of the hybridization between 3*d*- and 5*d*-electrons. The calculation with SOI was performed only within a perturbative treatment, evaluating the change in the energy level (ϵ_i). In Fe-X (X=Pd, Pt) alloy, transitions between the BCC, BCT, FCT, FCC are known depending on temperature and concentration of X; Fe(100-x)X(x) (X=Pd, Pt). Regarding the x-concentration, the combination with the rigid band approximation allows a better understanding of the percentage of elements (x) corresponding to a given number of electron states (or a Fermi energy shift).

3 Results

3.1 Magnetic moments

The total and atomic magnetic moments calculated by QSGW have a tendency to increase compared with GGA. This tendency is typical in QSGW [18,19]. As shown in Table II, values of the total magnetic moment become larger by 8~9 % than in our case of GGA. Focusing on the atomic magnetic moment, the atomic magnetic moments of Pd and Pt are larger in QSGW by about 12% and 5%, respectively, and in the case of Fe, the atomic magnetic moment increased by about 8%.

For Fe_3Pt, investigations using the QSGW method revealed that the calculated magnetic moment is overestimated relative to the experimental value of Ref. [31] by approximately 2%. This tendency for overestimation is also one of the characteristics of the QSGW approach, as it enhances the localization of magnetic moments due to its improved treatment of exchange and correlation effects. The observed discrepancy between the calculated and experimental magnetic moments may also be attributed to the inherent idealizations of the theoretical model. The present

Table II. Total magnetic moments [μ_B/f. u.] and atomic magnetic moments [μ_B/atom] in Fe_3X (X=Pd, Pt) obtained by QSGW an GGA approaches. The experimental values are also reported. The data with Ref. [33] was estimated as a limit of zero temperature from the temperature dependence of measured magnetization.

	Method	Magnetic moments [μ_B]		
		Total	Fe	X
Fe_3Pd	QSGW	9.45	3.09	0.36
	GGA: PBE	8.70	2.86	0.32
	GGA: PBE	8.45 [20] 8.56 [29]	2.74[29]	0.33[29]
Fe_3Pt	QSGW	9.16	2.97	0.41
	GGA: PBE	8.49	2.76	0.39
	GGA: PBE	8.44 [20] 8.0 [30]	2.5 [30]	0.5 [30]
	Exp.	9.0 (7 K) [31] 9.2 (77K) [32] 8.8 [33]	2.8 [32]	0.8 [32]

theoretical approach of QSGW assumes a defect-free crystal structure and neglects the effects of thermal fluctuations and structural inhomogeneities. Although the experimental value of Ref. [32] is slightly larger than the QSGW value, the authors reported the data with error bar and our QSGW calculation on magnetic moment does not contain the effect of SOI. Moreover, spin fluctuation as electron correlation effects [34] may be required for evaluating the magnetic moment more precisely in QSGW.

It is noted that the experimental magnetic moment for Fe_3Pt was compared with the theoretical prediction, as in Table II. This is because the alloy closely comparable to an ordered alloy was synthesized for Fe_3Pt. As a result, the QSGW indicates a better agreement with experimental data, compared with the GGA. In contrast, due to the difficulties in synthesizing ideal (stoichiometric and regular) Fe_3Pd, the theoretical data on the magnetic moment does not find any appropriate experimental counterpart for comparison. Alloying effects can be accessed by increasing the number of atoms in the computational cell as a future problem.

3.2 Total density of states

The total density of states (DOS) for Fe_3X (X=Pd, Pt) is presented in Fig. 2. The exchange splitting is clearly indicated, reflecting to the large magnetic moment in both alloys as presented in the previous subsection. The QSGW provides more spiky profile than the GGA as an overall feature. This is a consequence that electron localization effects were considered through the explicit inclusion of exchange-correlation potential in the QSGW method.

Here, we focus on the energy range near the Fermi level (see the inset in Fig. 2). For Fe_3Pd, a distinct peak at the Fermi level is noticeable in both QSGW and GGA. Moreover, for QSGW, another larger peak shifted by 0.1 eV above the Fermi level is noticeable in the total DOS. For Fe_3Pt of QSGW, the density of the peak close to the Fermi level is larger compared with the peak

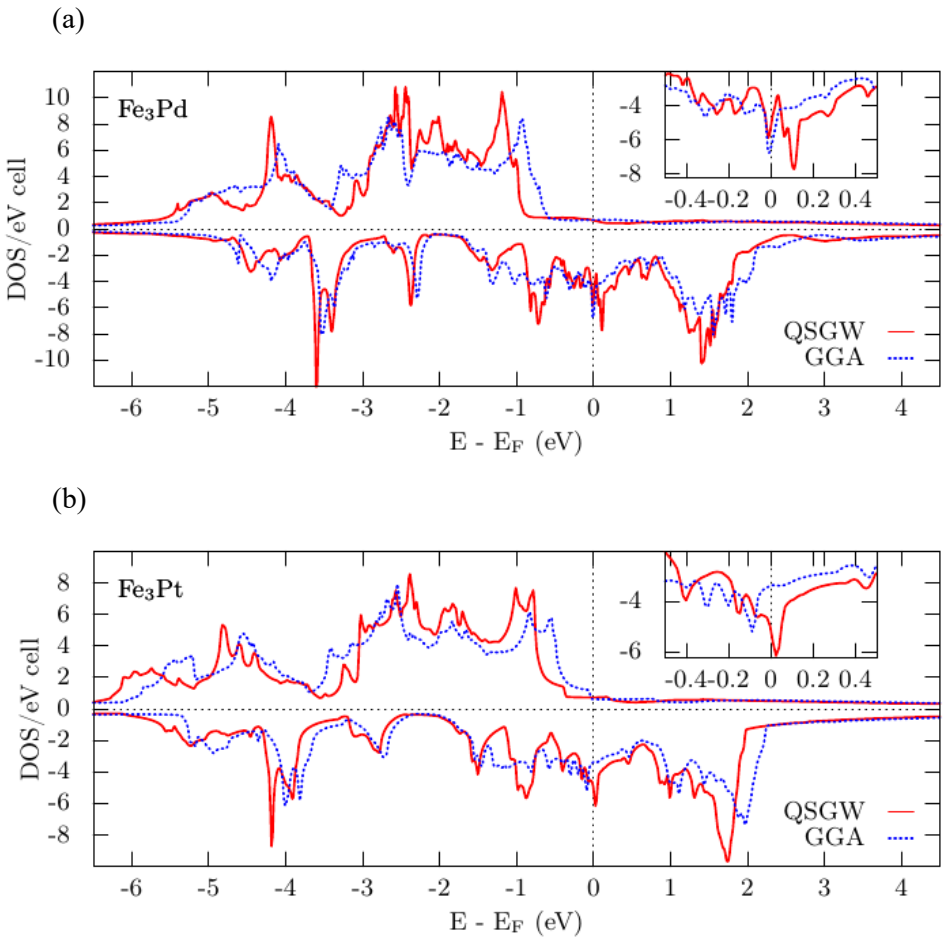

Fig. 2. Total density of states for Fe_3X: QSGW (solid red lines) and GGA (dashed blue lines). (a) X=Pd, (b) X=Pt. Positive DOS values are for majority-spin state and the negative for minority-spin state.

of GGA shifted by 0.1 eV to below the Fermi level. Such behavior of the peaks can correspond to a band Jahn-Teller effect which creates lower symmetry. The larger densities at the peaks in QSGW are a consequence of the band narrowing caused by the electron localization effect of *d*-orbitals. In QSGW, the common features observed both in Fe_3Pd and Fe_3Pt are summarized as the energy level shift of about 0.1 eV and the band narrowing when compared with GGA.

3.3 Band dispersion curves

For both Fe_3Pd and Fe_3Pt, the QSGW and GGA methods provide metallic behavior, with band crossings at the Fermi level appearing in various directions of the Brillouin zone, as shown in Fig. 3. The QSGW leads to a systematic shift of valence bands relative to the Fermi level. The bands with flat features close to Fermi level are observed around R points and along the lines from the R points to the directions of Γ, X, and M points for both alloys: at 0.1 eV through 0.2 eV for

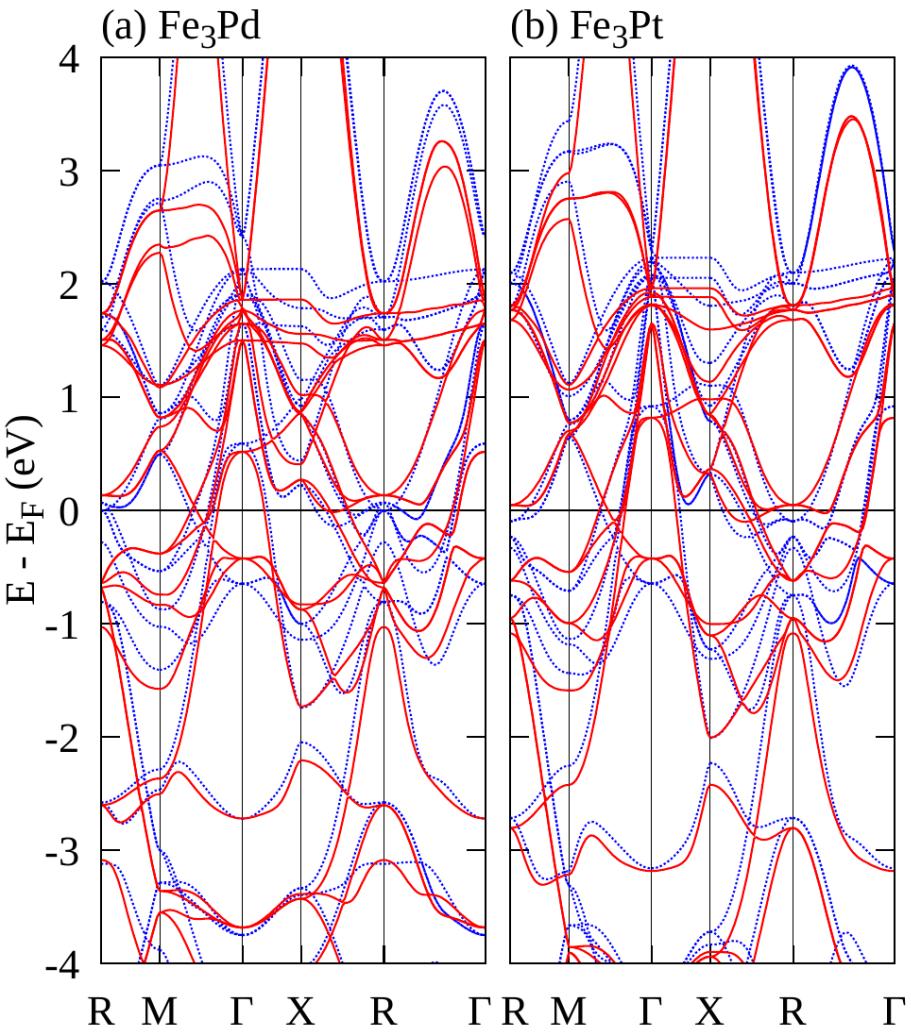

Fig. 3. Band dispersion curves for the minority-spin state: (a) Fe_3Pd; (b) Fe_3Pt for QSGW (red solid lines) and GGA (blue dotted lines).

Fe_3Pd and at vicinity just on the Fermi level for Fe_3Pd. In comparison with GGA, these band shifts to the higher energy around the vicinity of the Fermi level, corresponding to the larger exchange splitting, resulting in the larger magnetic moments in QSGW. Interestingly, in the energy ranges away from the Fermi level, around −4~−1 eV and 1~4 eV in Fig. 3, the band shift appears in the reversed direction as a lowering energy.

The differences observed between the alloys imply a subtle difference on *x*-concentration observed in the experimental data. The presence of flat bands can provide the instability of electronic structure, suggesting a potential relationship with the band Jahn-Teller effect, particularly due to the localized 3*d*-3*d*- and 3*d*-5*d*-hybridized electron system in these materials.

3.4 Partial density of states

Figures 4 and 5 show the projected components of the *d*-orbitals for the QSGW and GGA calculations, corresponding to Fe_3Pd and Fe_3Pt, respectively. In both alloys, the exchange splitting on Fe components is clearly indicated. For the component of X (Pd or Pt) atom, the intensity of the splitting looks larger in the component of $t_{2g}-$ orbitals than e_g-orbitals (see Figs. 4(a), 4(b), 5(a), and 5(b)). Since the angular directions in $t_{2g}-$orbitals are aligned to the neighboring Fe atoms, the large exchange splitting on Fe is reflected in the partial density of states (PDOS) for X atom through the orbital hybridization between Fe and X.

Analyzing the data from Fig. 4 (Fe_3Pd), for the base-centered Fe atom, the $t_{2g}-$ and e_g-orbitals on Fe provide a dominant contribution to the Fermi level, compared to the Pd atom. The local crystal field and hybridization remove the degeneracy of orbitals on Fe (see Figs. 4(c) and 4(d)). The component of $d_{yz}+d_{zx}$ orbitals exhibits different peak behavior in the vicinity of the Fermi level compared to d_{xy} orbital. It is the main contribution to the peak at 0.1 eV above the Fermi level. For e_g-orbitals, a lifting of the degeneracy between $d_{x^2-y^2}$ and $d_{3z^2-r^2}$ appears and the former also contributes to the peak at 0.1 eV. A similar trend was observed for Fe_3Pt, as shown in Fig. 5, where the local crystal field and hybridization also lead to the lifting of orbital degeneracy in $t_{2g}-$ and e_g-orbitals on Fe atom (see Figs. 5(c) and 5(d)). The orbital splitting obtained in our results implies an expected mechanism on the martensitic transformation related to band Jahn-Teller effects. This picture will be discussed in the Discussions section.

It is interesting to observe that the Pt peaks are located at the low energy by about 0.6 eV compared with those of Pd (see Figs. 4 (a), 4(b), 5(a), and 5(b)). This means that the Pt component tends to stay in the lower energy side than the Pt component with respect to the Fe component. Although these energy differences are much larger than the energy difference between Pt and Pd on the energy location of the band Jahn-Teller peak, which is addressed in the previous paragraph, the changing direction coincides with each other: the energy location of the band Jahn-Teller peak is lower in X=Pt than in X=Pd.

Situations obtained by GGA in electronic structure may be similar to those of QSGW. However, the energy location of the band Jahn-Teller peak is lowered in GGA since the energy lowering comes from the over-binding feature of electronic structure in GGA. Such a feature prohibits the quantitative argument on the instability of electronic states related to the vicinity of Fermi level. In this point of view, although the quantitative difference of energy looks small, the QSGW method significantly improves description of the electronic structures in the magnetic alloys of Fe_3Pd and Fe_3Pt.

In the next subsection, to treat the energy location of the band Jahn-Teller peak more quantitatively and to evaluate the generalized susceptibility under the rigid band approximation, the total DOS was integrated from the Fermi energy to some appropriate value.

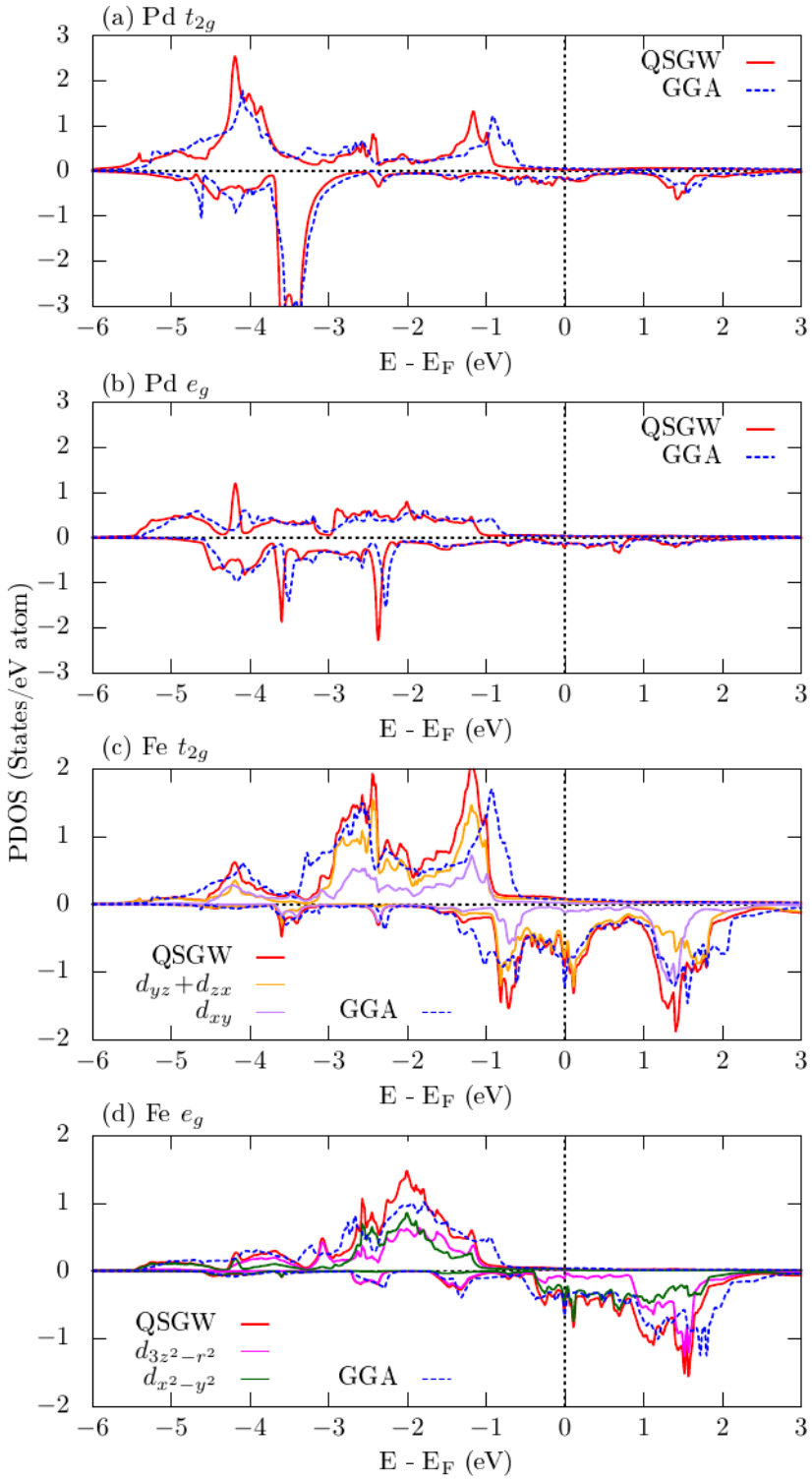

Fig. 4. Partial density of states (PDOS) in Fe_3Pd for QSGW (red solid lines) and GGA (blue dashed lines) projected to (a) Pd t_{2g}, (b) Pd e_g, (c) Fe t_{2g}, (d) Fe e_g. The components of $d_{yz}+d_{zx}$, d_{xy}, $d_{3z^2-r^2}$, and $d_{x^2-y^2}$ refer to the text. Positive PDOS values are for majority-spin state and negative for minority-spin state.

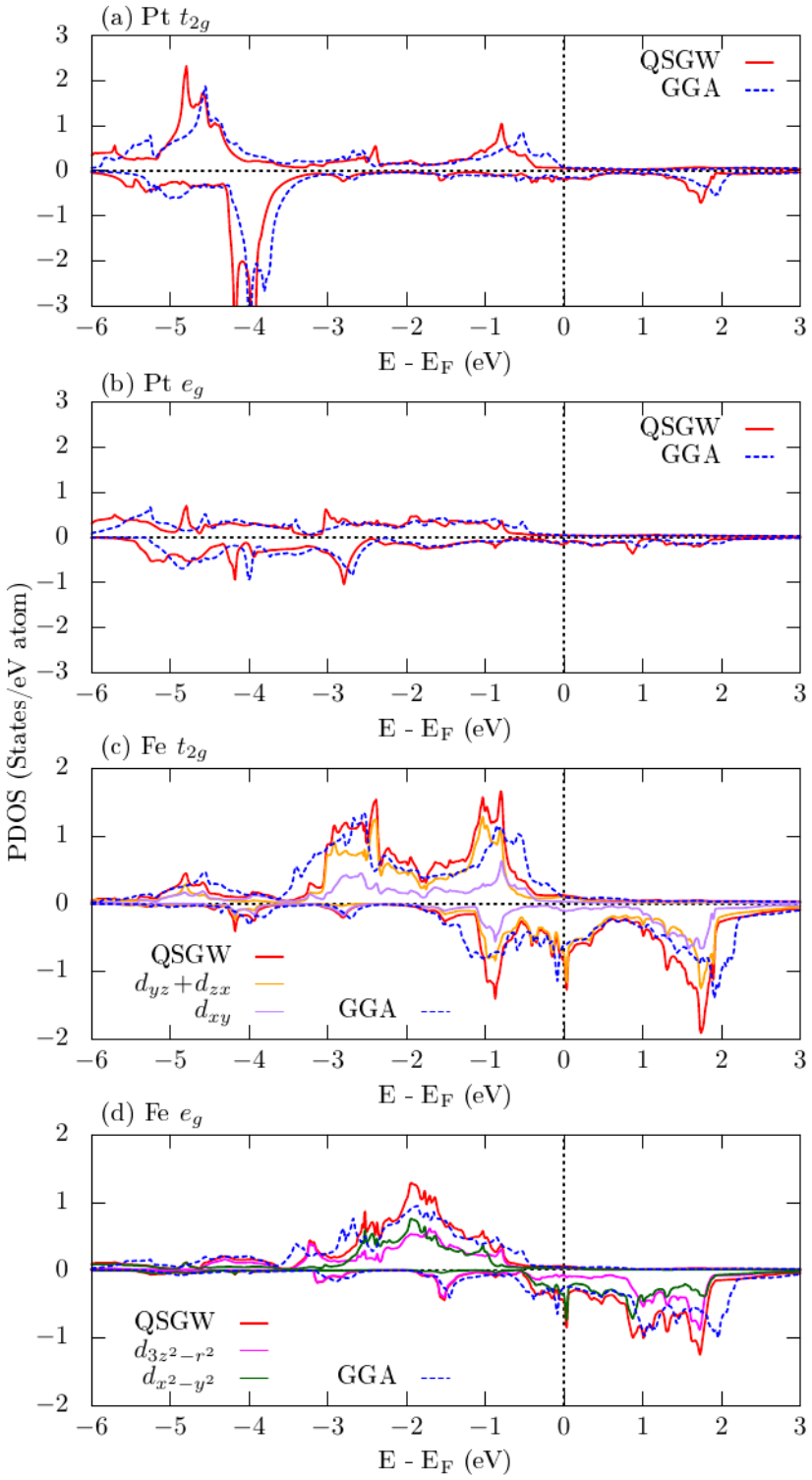

Fig. 5. Partial density of states (PDOS) in Fe_3Pt for QSGW (red solid lines) and GGA (blue dashed lines) calculations projected to (a) Pt t_{2g}, (b) Pt e_g, (c) Fe t_{2g}, (d) Fe e_g. The components of $d_{yz}+d_{zx}$, d_{xy}, $d_{3z^2-r^2}$, and $d_{x^2-y^2}$ refer to the text. Positive PDOS values are for majority-spin state and negative for minority-spin state.

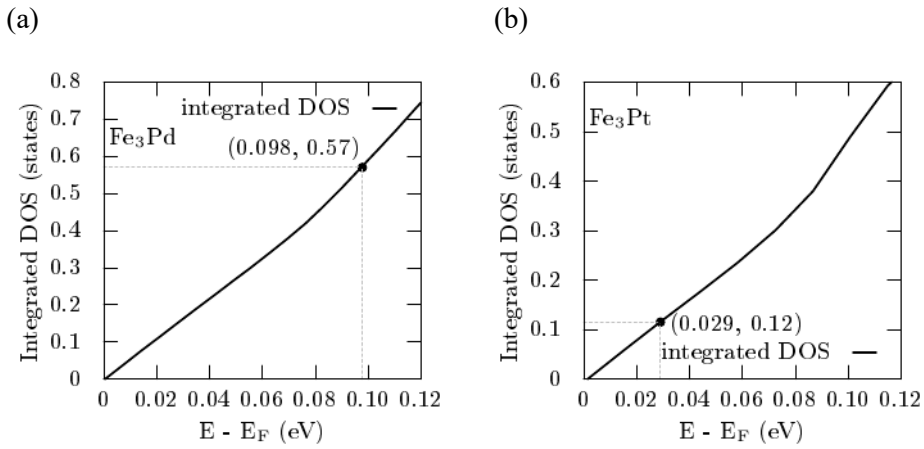

Fig. 6. The increasing number of electrons with respect to the positive energy shift in vicinity of the Fermi level for (a) Fe_3Pd and (b) Fe_3Pt. The point symbol indicates the position corresponding to the maximum value in $\chi(\boldsymbol{q})$.

3.5 Relation between the number of electrons and Fermi energy shift

Figure 6 shows the increasing number of electrons estimated by the integration of total DOS for Fe_3Pd and Fe_3Pt. The horizontal axis specifies an energy shift of the Fermi energy in the rigid band approximation, while the vertical axis, namely integrated value, indicates the increased number of electrons in one formula unit (unit cell). As an example shown in Fig. 6(a), under the rigid band approximation, the energy shift of 0.098 eV corresponds to the additional 0.57 electrons in the unit cell, which is compiled to the alloy concentration of x=32.12, while the origin of Fig. 6 corresponds to the alloy concentration of x=25.

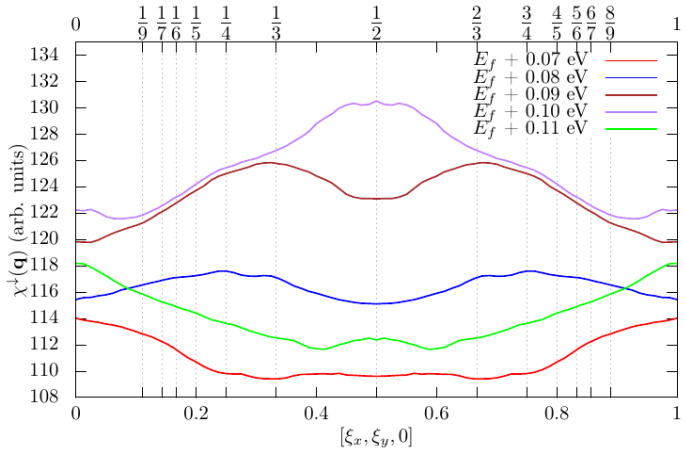

Fig. 7. Profile of the QSGW generalized susceptibility of the minority-spin component $\chi^{\downarrow}(\boldsymbol{q})$ in Fe_3Pd along the $[1,1,0]$ direction from the origin, depending on shift ($\Delta E_F = 0.07 - 0.11$ eV) from the Fermi level.

3.6 Generalized susceptibility

Using the rigid band approximation, the generalized susceptibility $\chi(\boldsymbol{q})$ was evaluated for a given Fermi energy shift ΔE_{F} and a given wave vector $\boldsymbol{q} = \frac{2\pi}{a}(\xi_x, \xi_y, \xi_z)$ in both alloys, Fe_3Pd and Fe_3Pt. As the results, we found that $\chi(\boldsymbol{q})$ took the maximum at $\Delta E_{\mathrm{F}} = 0.098$ eV in Fe_3Pd and at $\Delta E_{\mathrm{F}} = 0.029$ eV in Fe_3Pt, respectively, as referred in Fig. 6. For the maximum value, the corresponding wave vectors were determined as $\boldsymbol{q} = (2\pi/a)(1/2,1/2,0)$ for Fe_3Pd and $\boldsymbol{q} = (2\pi/a)(1/8,1/8,0)$ for Fe_3Pt, respectively. The details of profile on $\chi(\boldsymbol{q})$ are presented and explained in the following subsections.

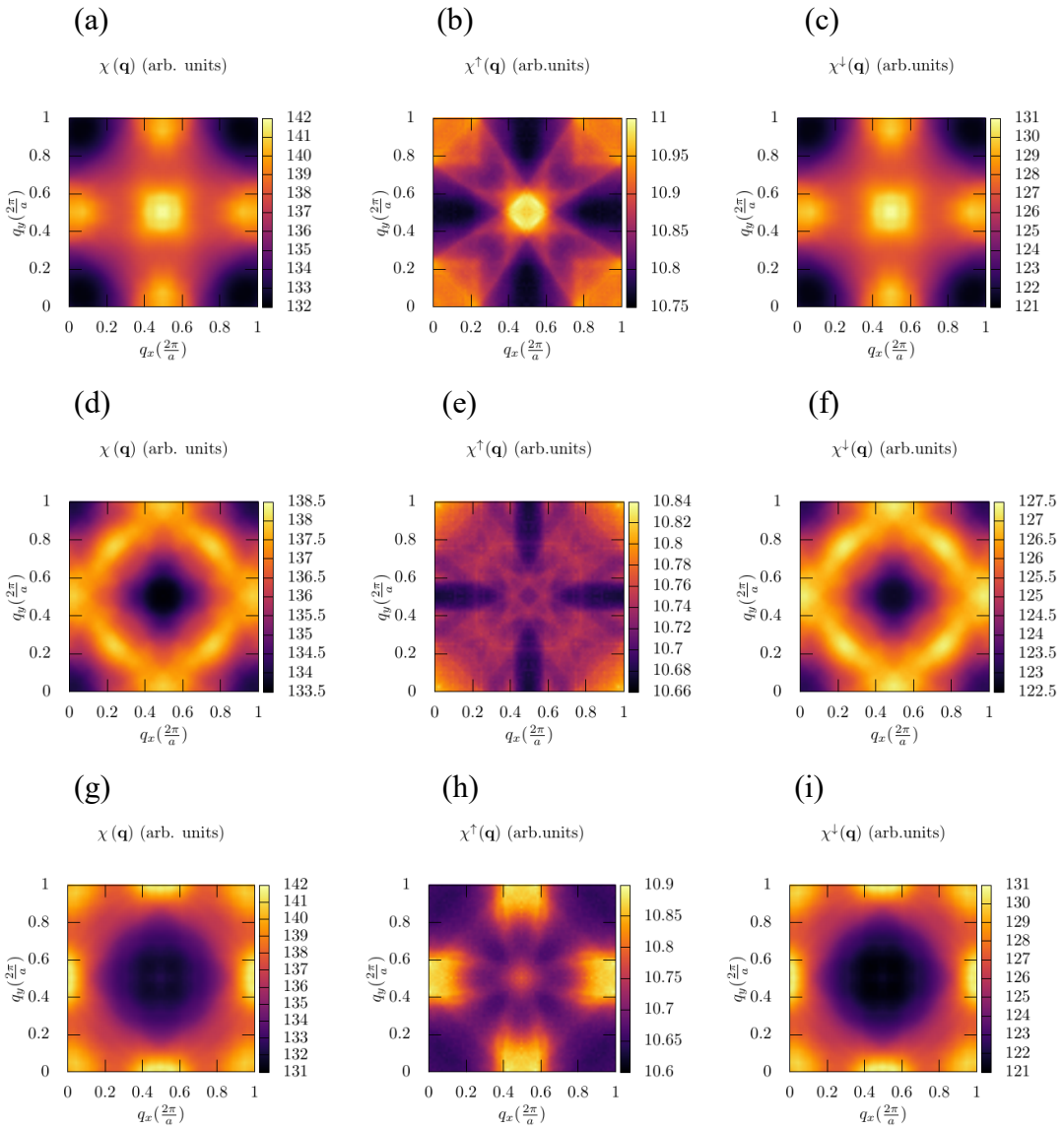

Fig. 8. QSGW generalized susceptibility at $\Delta E_{\mathrm{F}} = 0.098$ eV in Fe_3Pd: total $\chi(\boldsymbol{q})$, majority-spin $\chi^{\uparrow}(\boldsymbol{q})$, and minority-spin $\chi^{\downarrow}(\boldsymbol{q})$ components with (a)-(c) within the plane of $q_z = 0$; (d)-(f) within $q_z = \left(\frac{2\pi}{a}\right) \times \frac{1}{4}$; (g)-(i) within $q_z = \left(\frac{2\pi}{a}\right) \times \frac{1}{2}$.

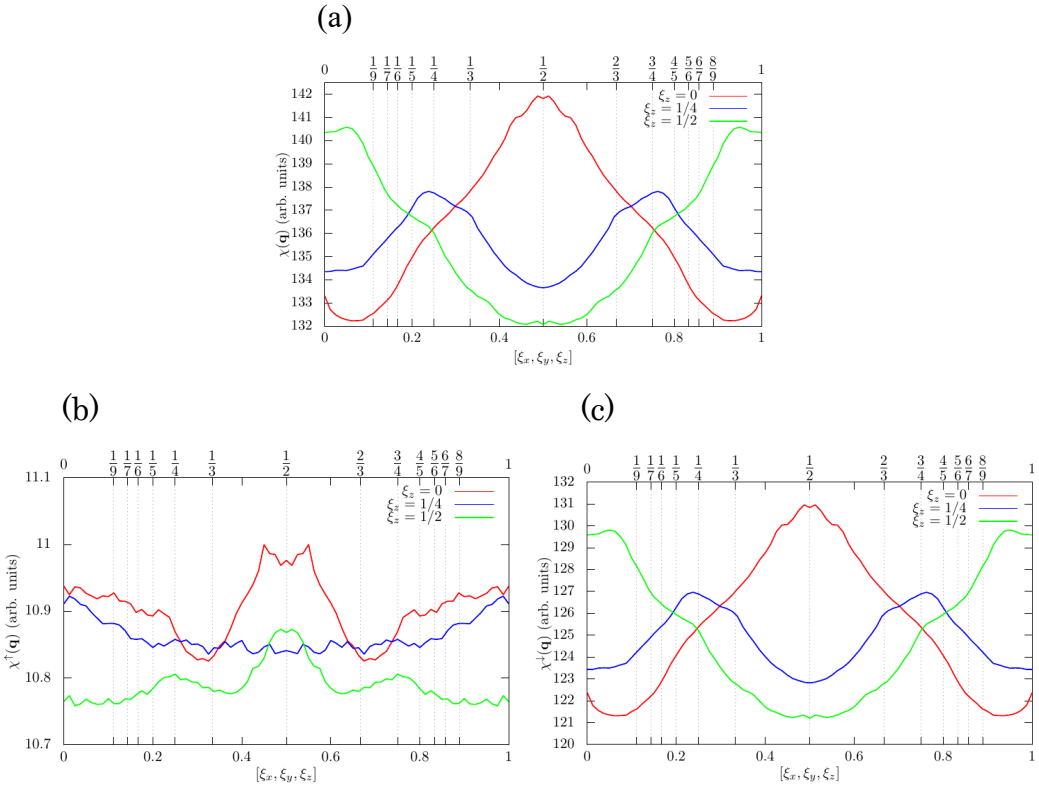

Fig. 9. Profile of the QSGW generalized susceptibility along the [1, 1, 0] direction at $\Delta E_F = 0.098$ eV in Fe_3Pd: (a) total $\chi(\boldsymbol{q})$, (b) majority-spin $\chi^{\uparrow}(\boldsymbol{q})$, and (c) minority-spin $\chi^{\downarrow}(\boldsymbol{q})$ components at $[\xi_x, \xi_y, \xi_z]$.

3.6.1 Fe_3Pd alloy

The generalized susceptibility contributed from intra-band takes a value proportional to the DOS at the Fermi level for $\boldsymbol{q} = 0$. Thus, considering the smaller (larger) DOS at the Fermi level in the majority-spin (minority-spin) state, this implies a larger contribution from the minority-spin state and the data is sometimes presented only for the minority-spin state. Indeed, in all the cases investigated here for $\chi(\boldsymbol{q})$, the contribution from the minority-spin state $\chi^{\downarrow}(\boldsymbol{q})$ is always dominant.

Figure 7 shows $\chi^{\downarrow}(\boldsymbol{q})$ along the $[1,1,0]$ direction from $\boldsymbol{q} = 0$ to $\boldsymbol{q} = (2\pi/a)(1,1,0)$. $\chi^{\downarrow}(\boldsymbol{q})$ takes a maximum around $\Delta E_F = 0.10$ eV at $\boldsymbol{q} = (2\pi/a)(1/2,1/2,0)$. In the more precise search, the maximum was determined at $\Delta E_F = 0.098$ eV at the same wave vector $\boldsymbol{q}$ (see Fig. A1 in Appendix A). In Figs. 8 and 9, the behaviors of $\chi(\boldsymbol{q}) = \chi^{\uparrow}(\boldsymbol{q}) + \chi^{\downarrow}(\boldsymbol{q})$, $\chi^{\uparrow}(\boldsymbol{q})$, and $\chi^{\downarrow}(\boldsymbol{q})$ in the BZ are presented as contour maps and line profiles, respectively, at $\Delta E_F = 0.098$ eV. In these figures, the specified q_z is introduced: $q_z = 0$, $q_z = \left(\frac{2\pi}{a}\right) \times 1/4$, and $q_z = \left(\frac{2\pi}{a}\right) \times 1/2$. The contour maps were drawn within the *xy*-plane and the line profiles were plotted along the $[1,1,0]$ direction. As explicitly indicated, contributions of the minority-spin state are always dominant, and the contribution from the majority-spin state does not influence to its relative distribution in the BZ in so large extent. As seen in Figs. 8 and 9, the second maxima are found at around $\boldsymbol{q} = (2\pi/a)(1/2,0,0)$, although, strictly speaking, the position of these

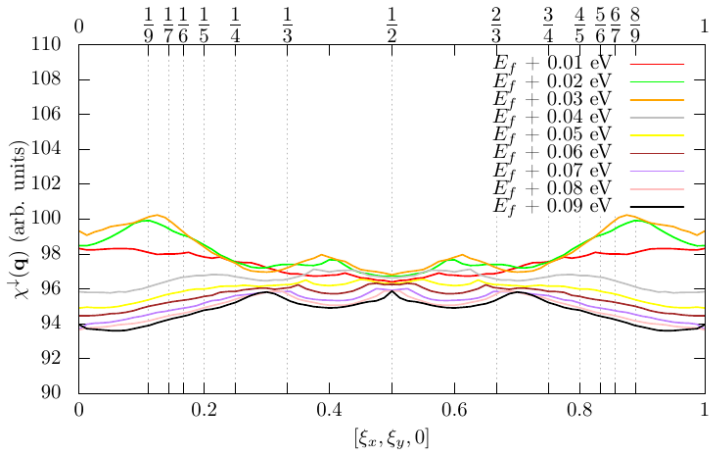

Fig. 10. Profile of the QSGW generalized susceptibility of the minority-spin component $\chi^{\downarrow}(\boldsymbol{q})$ in Fe_3Pt along the $[1,1,0]$ direction from the origin, depending on shift $(\Delta E_{\mathrm{F}} = 0.01 - 0.09\ \mathrm{eV})$ from the Fermi level.

maxima are not just on it.

In Appendix B, for the reader's convenience, the behaviors of $\chi(\boldsymbol{q}) = \chi^{\uparrow}(\boldsymbol{q}) + \chi^{\downarrow}(\boldsymbol{q})$, $\chi^{\uparrow}(\boldsymbol{q})$, and $\chi^{\downarrow}(\boldsymbol{q})$ in the BZ are also presented as contour maps and line profiles at $\Delta E_{\mathrm{F}} = 0$, as in Figs. 8 and 9.

3.6.2 Fe_3Pt alloy

Figure 10 shows $\chi^{\downarrow}(\boldsymbol{q})$ along the $[1,1,0]$ direction from $\boldsymbol{q} = 0$ to $\boldsymbol{q} = (2\pi/a)(1,1,0)$. $\chi^{\downarrow}(\boldsymbol{q})$ takes maxima around $\Delta E_{\mathrm{F}} = 0.03$ eV. In the more precise research, the maxima were determined at $\Delta E_{\mathrm{F}} = 0.029$ eV at $\boldsymbol{q} = (2\pi/a)(1/8,1/8,0)$ (see Fig. A2 in Appendix A). As the same for Fe_3Pd, in Figs. 11 and 12, the behavior in the BZ is presented as contour maps and line profiles, respectively, at $\Delta E_{\mathrm{F}} = 0.029$ eV. Even the second maxima did not appear at around $\boldsymbol{q} = (2\pi/a)(1/2,0,0)$, unlike the case of Fe_3Pd.

3.6.3 Effects of spin-orbit interaction in Fe_3Pt alloy

The inclusion of SOI for Fe_3Pt modifies the electronic states in vicinity of the Fermi level due to a large SOI interaction on Pt atom through the hybridization between Fe and Pt. The modification near Fermi level is important in the relation with system stability. The differences introduced by SOI are sometimes crucial for explaining spin-dependent electronic properties in Fe_3Pt. It is found that the energy scale from -0.5 to 0.5 eV around the Fermi level shows noticeable differences between the cases with and without SOI. In the case of SOI, as shown in Fig. 13, the peak on the Fermi level was observed for the QSGW with SOI. However, the amplitude of the peak is lowered compared with the case without SOI. Such phenomena may be related to the redistribution of states due to SOI. The set of obtained band energies allows us to evaluate the generalized susceptibility $\chi(\boldsymbol{q})$. In Appendix C, the resulting distribution of $\chi(\boldsymbol{q})$ is reported for future convenience. This can imply candidates for the modulation wave vector $\boldsymbol{q}$ of FSN.

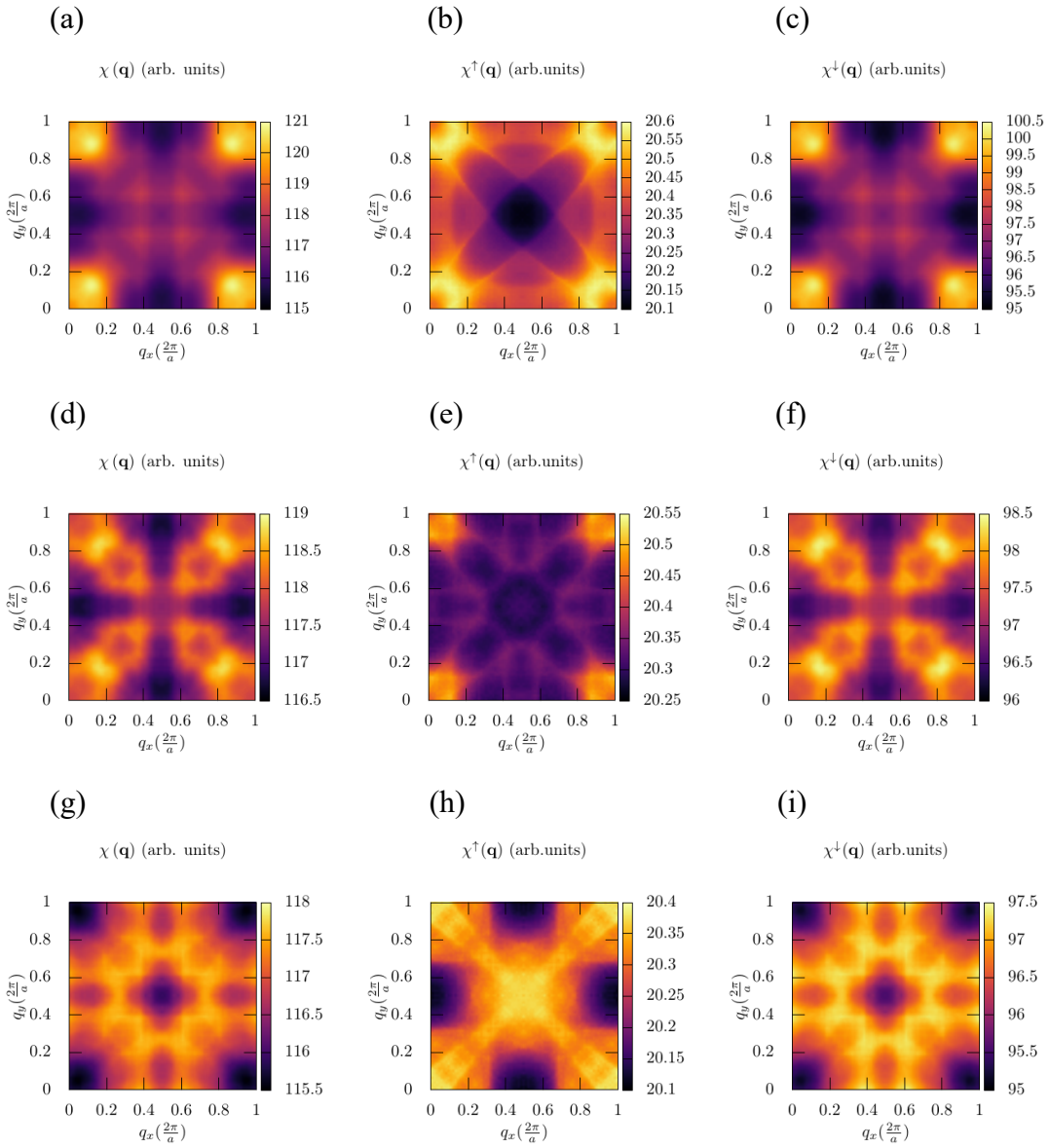

Fig. 11. QSGW generalized susceptibility at $\Delta E_F = 0.029$ eV in Fe_3Pt: total $\chi(\boldsymbol{q})$, majority-spin $\chi^{\uparrow}(\boldsymbol{q})$, and minority-spin $\chi^{\downarrow}(\boldsymbol{q})$ components with (a)-(c) within the plane of $q_z = 0$; (d)-(f) within $q_z = \left(\frac{2\pi}{a}\right) \times \frac{1}{4}$; (g)-(i) within $q_z = \left(\frac{2\pi}{a}\right) \times \frac{1}{2}$.

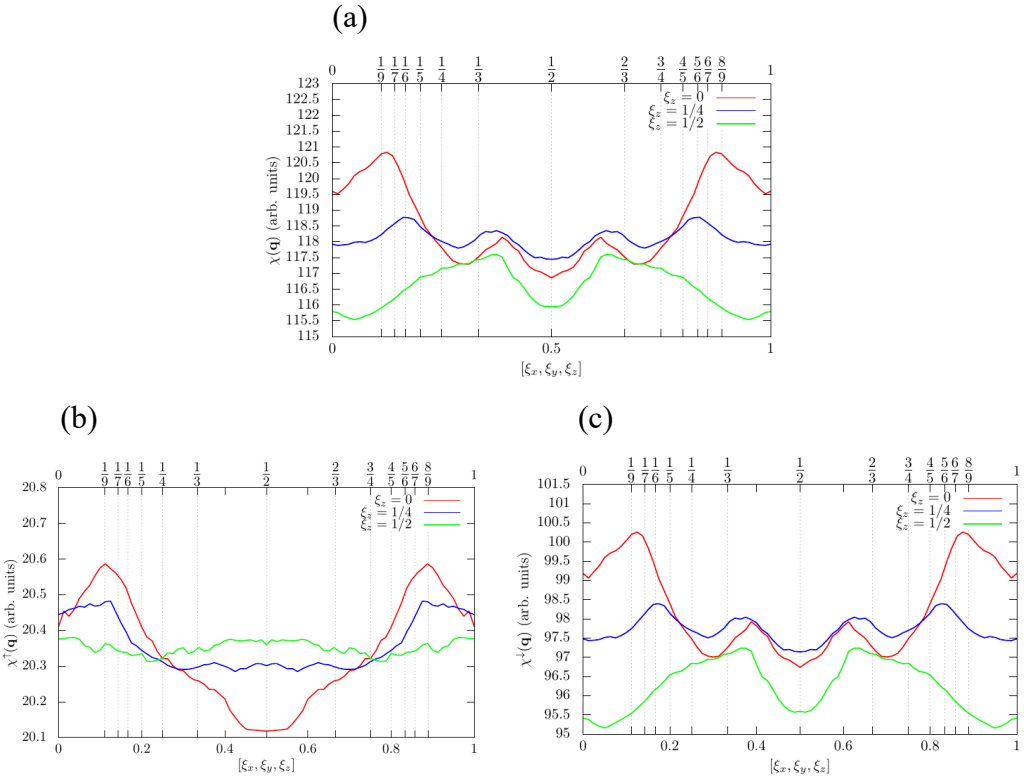

Fig. 12. Profile of the QSGW generalized susceptibility along the [1, 1, 0] direction at $\Delta E_{\mathrm{F}} = 0.029$ eV in Fe_3Pt: (a) total $\chi(\boldsymbol{q})$, (b) majority-spin $\chi^{\uparrow}(\boldsymbol{q})$, and (c) minority-spin $\chi^{\downarrow}(\boldsymbol{q})$ components at $[\xi_x, \xi_y, \xi_z]$.

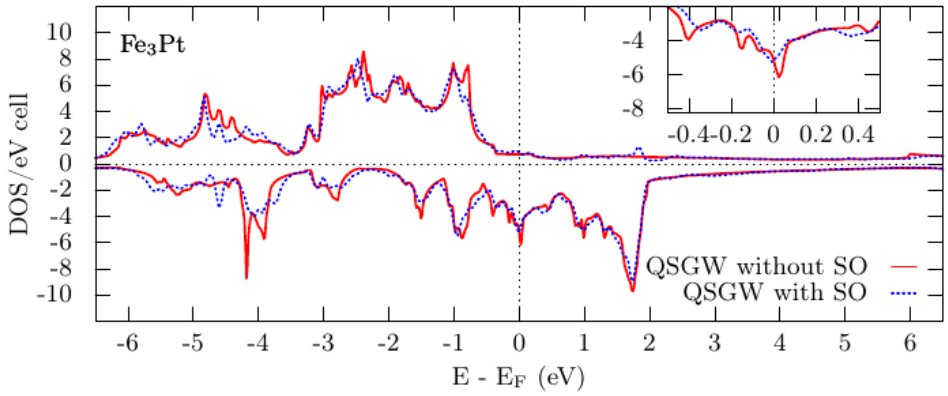

Fig. 13. Total density of states: QSGW without SOI (solid red lines) and with SOI (dashed blue lines) for Fe_3Pt. Positive DOS values are for majority-spin state and the negative for minority-spin state.

4 Discussions

It is interesting to see the differences between Fe_3Pd and Fe_3Pt. Regarding the theoretical total magnetic moments, the X=Pd case indicated a larger one than that of X=Pt (see Table II). The Fe moment for X=Pd is also larger than that for X=Pt, but the X moment has an inverse trend. This means that the Pt moment is larger than the Pd one. Regarding the DOS (for example, see Figs. 4 and 5), the Pt energy levels tend to be deeper than those of the Pd ones. Reflecting such trend, the Fe 3*d*-orbital minority-spin states may be drawn to lower energies for X=Pt and to high energies for X=Pd. Namely, the Fe magnetic moment in X=Pd is larger than in X=Pt in consequence of the trend of exchange splitting (see Fig. 2). According to this trend between Pt and Pd, the highest peaks in the generalized susceptibility (or FSN) appear at the smaller *x*-concentration in X=Pt and at the larger *x*-concentration in X=Pd.

Using the rigid band approximation and integrated DOS data, a Fermi energy shift of +0.098 eV from the Fermi level ($\Delta E_{\mathrm{F}} = 0.098$ eV) predicts a chemical composition of $Fe_{67.88}Pd_{32.12}$ (x=32.12). The analysis of generalized susceptibility data (Figs. 8 and 9), incorporating this Fermi energy shift, suggests the potential for a martensitic transformation. The peak observed along $[\xi, \xi, 0]$ with ξ=1/2 suggests the likelihood of tetragonal distortion due to strong nesting effects. As discussed in the previous work [20], the phonon soft mode can couple with the electronic instability specified by the modulation wave vector at $\boldsymbol{q} = (2\pi/a)(1/2,1/2,0)$. The pronounced FSN observed in the generalized susceptibility peaks for $Fe_{67.88}Pd_{32.12}$ aligns with their predicted tendency for tetragonal distortion, as previously discussed in the context of the phase diagram [12]. Our results further support the role of FSN in driving martensitic transformations in Fe-Pd alloys.

For the alloy Fe(100-x)Pt(x), the rigid band approximation and integrated DOS data, as for the Fe-Pd alloy, the energy shift +0.029 eV from the Fermi level ($\Delta E_{\mathrm{F}} = 0.029$ eV) predicts a chemical composition of $Fe_{73.5}Pt_{26.5}$ (x=26.50). The generalized susceptibility data (Figs. 11 and 12), reflecting this energy shift, suggests the possibility of structural instability in $Fe_{73.5}Pt_{26.5}$. The peaks observed at $\boldsymbol{q} = (2\pi/a)(1/8,1/8,0)$ for this composition indicate a potential tetragonal driving by pronounced nesting effects. However, this $\boldsymbol{q}$-vector is much smaller than those of the Fe-Pd system obtained here and cannot be connected directly to the tetragonal distortion discussed in the experiment [13]. To speculate about this discrepancy, two reasons can be raised as important. One may originate from the smallness of $\boldsymbol{q} = (2\pi/a)(1/8,1/8,0)$ which corresponds to a longer wavelength. Thus, satellite diffraction peaks of some main peak or small angle diffraction line/spot can be expected in the X-ray diffraction measurement. Another one is the SOI. In the present work, unfortunately, such interaction was not exactly introduced in the calculation of generalized susceptibility.

In Fe_3Pt, the DOS peak related to the band Jahn-Teller effect appears close to the Fermi level (see Figs. 2 and 13). As speculated from Fig. C1, if the FSN is caused at $\boldsymbol{q} = (2\pi/a)(1/2,0,0)$, the multiple instability combined with the vectors of $\boldsymbol{q}_1 = (2\pi/a)(1/2,0,0)$ and $\boldsymbol{q}_2 = (2\pi/a)(0,1/2,0)$ can realize a tetragonal distortion: $\boldsymbol{q}_1 + \boldsymbol{q}_2 = (2\pi/a)(1/2,1/2,0)$, as obtained in the present work for Fe_3Pd. In any way, the advanced inclusion of SOI may be an issue that stands against the alloy containing heavy elements.

This work suggested the instability at x=32.12 for X=Pd and at x=26.50 for X=Pt for the alloy Fe(100-x)X(x). According to the rigid band approximation, in which the integration of DOS was performed for each spin state, the total magnetic moment was deduced at these instability points: 8.98 μ_{B}/f. u. (=9.45−0.47) for X=Pd, 9.08 μ_{B}/f. u. (=9.16−0.08) for X=Pt.

Associated with the martensitic transformation, the band Jahn-Teller effect usually plays one of the important roles. The band energy states located at the Fermi level take an energy splitting below and above the Fermi energy at the transformation, resulting in a local atomic distortion. Such a structure is determined by the electronic structure of high symmetry phase, namely, the cubic phase in this work. As obtained in the results of PDOS (Figs. 4 and 5), the $d_{yz} + d_{zx}$ and $d_{x^2-y^2}$ orbitals on the Fe take part in the expected local structural change. Speculating the distances of the Fe with the neighboring Fe atoms (see Fig. 1), the $d_{yz} + d_{zx}$ tends to take the anti-bonding hybridization and the $d_{x^2-y^2}$ remains non-bonding after the transformation. These are similar to the energy splitting of Ni 3d e_g −orbitals located on the Fermi level in the cubic phase in Ni_2MnGa [18], separating to the above ($d_{x^2-y^2}$) and below ($d_{3z^2-r^2}$) the Fermi level in the tetragonal phase.

5 Conclusions

The analyses of the electronic structure, such as total and partial DOSs, band dispersion curves, and generalized susceptibility, were investigated in the cubic regular alloy Fe_3X (X=Pd, Pt) by using quasi-particle self-consistent *GW* (QSGW) method. For both alloys, the result of DOS indicated peak structures at vicinity of the Fermi level in the minority-spin state, attributing to the flat band nature around the saddle points in the BZ. The accurate procedure of QSGW provided the peaks located at higher energy with respect to the Fermi level, although they have been observed below the Fermi level in the GGA. From the combined analysis of generalized susceptibility and rigid band approximation, the expected instability by lattice modulation was found to occur at the system containing more electrons compared with the stoichiometric alloy. This occurrence corresponds to 32.12 atomic % Pd (x=32.12) for Fe_3Pd or 26.50 atomic % Pt (x=26.50) for Fe_3Pt. These concentrations obtained at present work agree well with those of the available experimental values for the corresponding alloys. The profiles of generalized susceptibility indicated peak at the modulation wave vector $\boldsymbol{q} = (2\pi/a)(1/2,1/2,0)$ for x=32.12 in Fe(100-x)Pd(x) and $\boldsymbol{q} = (2\pi/a)(1/8,1/8,0)$ for x=26.50 in Fe(100-x)Pt(x).

The location of the Fermi energy determined in QSGW was moved by the shift of about 0.1 eV for both X=Pd and Pt, compared with those in GGA. Such accuracy of energy level determination in the electronic structure calculation may enable us to discuss a quantitative position of x-concentration regarding the boundary of the martensitic phase transition. The electronic structure calculation QSGW may provide such kind of accuracy in metallic systems.

Acknowledgments

The authors thank the researcher, Takao Kotani, for providing the code package *ecalj* and its details. The author (A.A.) acknowledges the researchers, Jakub Luštinec, and Rinku Majumder for their help in the initial stage of computation and the JST SPRING, Grant Number JPMJSP2135, project at Kanazawa University. The computation in this work was performed using the facilities of the Supercomputer Center, Institute for Solid State Physics (ISSP), the University of Tokyo, Japan. This work was partly supported by Japan Society for the Promotion of Science KAKENHI, Grant-in-Aid for Scientific Research (Nos. 21K04864, 21KK0083, 24K08229, 24K17608).

References

[1] K. Ullakko, J. K. Huang, C. Kantner, R. C. O'Handley, and V. V. Kokorin, Appl. Phys. Lett., **69**, 1966 (1996).
[2] A. V. Irzhak, D. I. Zakharov, V. S. Kalashnikov, V. V. Koledov, D. S. Kuchin, G. A. Lebedev, P. V. Lega, E. P. Perov, N. A. Pikhtin, V. G. Pushin, I. S. Tarasov, V. V. Khovailo, V. G. Shavrov, and A. V. Shelyakov, J. Commun. Technol. Electron., **55**, 818 (2010).
[3] H. E. Karaca, I. Karaman, B. Basaran, Y. Ren, Y. I. Chumlyakov, and H. J. Maier, Adv. Funct. Mater., **19**, 983 (2009).
[4] X. Zhang and M. Qian, (Magnetic shape memory alloys: preparation, martensitic transformation and properties, Springer Singapore, 2022), pp.165.
[5] H. Seiner, M. Zelený, P. Sedlák, L. Straka, and O. Heczko, Phys. Status Solidi RRL, **16**, 2100632 (2022).
[6] M. Zelený, P. Sedlák, O. Heczko, H. Seiner, P. Veřtát, M. Obata, T. Kotani, T. Oda, and L. Straka, Mater. Des., **209**, 109917 (2021).
[7] T. Sakamoto, T. Fukuda, T. Kakeshita, T. Takeuchi, and K. Kishio, J. Appl. Phys., **93**, 8647 (2003).
[8] X. Moya, L. Mañosa, A. Planes, T. Krenke, M. Acet, M. Morin, J. L. Zarestky, and T. A. Lograsso, Phys. Rev. B, **74,** 024109 (2006).
[9] H. Morito, A. Fujita, K. Fukamichi, R. Kainuma, K. Ishida, and K. Oikawa, Appl. Phys. Lett., **83**, 4993 (2003).
[10] H. Morito, K. Oikawa, A. Fujita, K. Fukamichi, R. Kainuma, and K. Ishida, Scr. Mater., **63**, 379 (2010).
[11] M. Matsui, K. Adachi, T. Shimizu, and H. Yamada, J. Magn. Soc. Jpn., **5**, 1201 (1981).
[12] M. Sugiyama, R. Oshima, and F. E. Fujita, Trans. Jpn. Inst. Met., **27**, 719 (1986).
[13] S. Muto, R. Oshima, and F. E. Fujita, Met. Trans., **19**, 2723 (1988).
[14] P. Ziesche, S. Kurth, and J. P. Perdew**,** Comput. Mater. Sci., **11**, 122 (1998).
[15] T. Mahmood, C. Cao, R. Ahmed, M. A. Saeed, and M. Ahmed, J. Optoelectron. Adv. Mater., **16**, 117 (2014).
[16] C. Loschen, J. Carrasco, K. M. Neyman, and F. Illas, Phys. Rev. B, **75**, 035115 (2007).
[17] M. S. Hybertsen and S. G. Louie, Phys. Rev. B, **34**, 5390 (1986).
[18] M. Obata, T. Kotani, and T. Oda, Phys. Rev. Mater., **7**, 024413 (2023).
[19] J. Luštinec, M. Obata, R. Majumder, K. Hyodo, T. Kotani, L. Kalvoda, and T. Oda, J. Magn. Soc. Jpn., **48**, 94 (2024).
[20] M. E. Gruner, W. A. Adeagbo, A. T. Zayak, A. Hucht, and P. Entel, Phys. Rev. B, **81**, 064109 (2010).
[21] S. V. Faleev, M. van Schilfgaarde, and T. Kotani, Phys. Rev. Lett., **93**, 126406 (2004).
[22] M. van Schilfgaarde, T. Kotani, and S. V. Faleev, Phys. Rev. Lett., **96**, 226402 (2006).
[23] T. Kotani, M. van Schilfgaarde, and S. V. Faleev, Phys. Rev. B, **76**, 165106 (2007).
[24] M. van Schilfgaarde, T. Kotani, and S. V. Faleev, Phys. Rev. B, **74**, 245125 (2006).
[25] R. A. Stern, S. D. Willoughby, J. M. MacLaren, J. Cui, Q. Pan, and R. D. James, J. Appl. Phys., **93**, 8644 (2003).
[26] Y. Liu, Y. Jiang, X. Zhang, Y. Wang, Y. Zhang, H. Liu, H. Zhai, Y. Liu, J Yang, and Y. Yan, J. Solid State Chem., **209**, 69 (2014).
[27] J. P. Perdew, K. Burke, and M. Ernzerhof, Phys. Rev. Lett., **77**, 3865 (1996).
[28] Ecalj, [online]. Available: https://github.com/tkotani/ecalj/ (As of December, 2024).

[29] G. L. Yu, T. M. Cheng, X. X. Zhang, and W. J. Gong, J. Magn. Magn. Mater., **538**, 168322 (2021).
[30] A. Hasegawa, J. Phys. Soc. Jpn., **54**, 1477 (1985).
[31] K. J. Kim, S. J. Lee, T. A. Wiener, and D. W. Lynch, J. Appl. Phys., **89**, 244 (2001).
[32] Y. Ishikawa, K. Tajima, Y. Noda, and N. Wakabayashi, J. Phys. Soc. Jpn., **48**, 1097 (1980).
[33] T. Sasaki and S. Chikazumi, J. Phys. Soc. Jpn., **46**, 1732 (1979).
[34] Y. Takahashi, J. Phys. Soc. Jpn., **55**, 3553 (1986).

Appendix A

The precise search of maximum value on the generalized susceptibility of the minority-spin component $\chi^{\downarrow}(\boldsymbol{q})$ is shown in Figs. A1 and A2 for Fe_3Pd and Fe_3Pt, respectively.

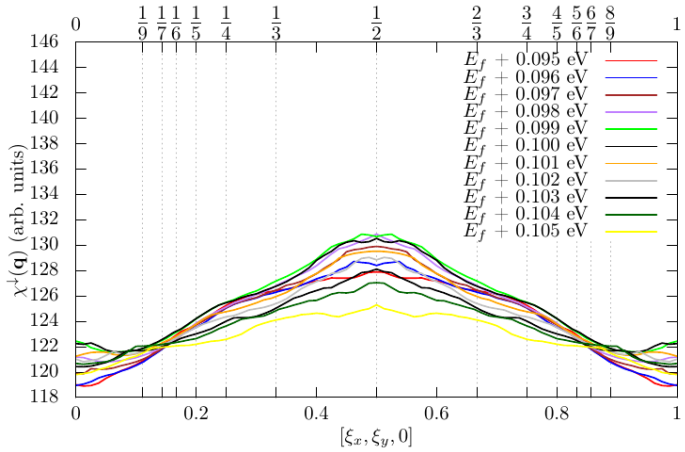

Fig. A1. Profile of the QSGW generalized susceptibility of the minority-spin component $\chi^{\downarrow}(\boldsymbol{q})$ in Fe_3Pd along the $[1,1,0]$ direction from the origin, depending on shift ($\Delta E_{\mathrm{F}} = 0.095 - 0.105$ eV) from the Fermi level.

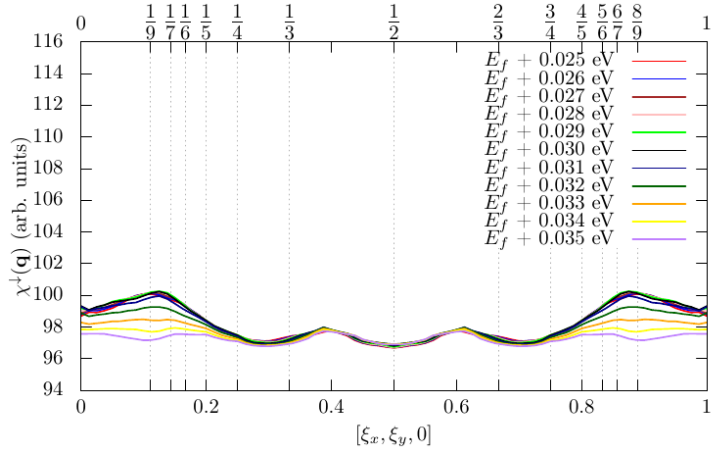

Fig. A2. Profile of the QSGW generalized susceptibility of the minority-spin component $\chi^{\downarrow}(\boldsymbol{q})$ in Fe_3Pt along the $[1,1,0]$ direction from the origin, depending on shift ($\Delta E_{\mathrm{F}} = 0.025 - 0.035$ eV) from the Fermi level.

Appendix B

The profiles of generalized susceptibility for the electronic structures in the self-consistent solutions ($\Delta E_{\mathrm{F}} = 0$): contour maps (Fig. B1) and line profiles (Fig. B2) in Fe_3Pd and contour maps (Fig. B3) and line profiles (Fig. B4) in Fe_3Pt.

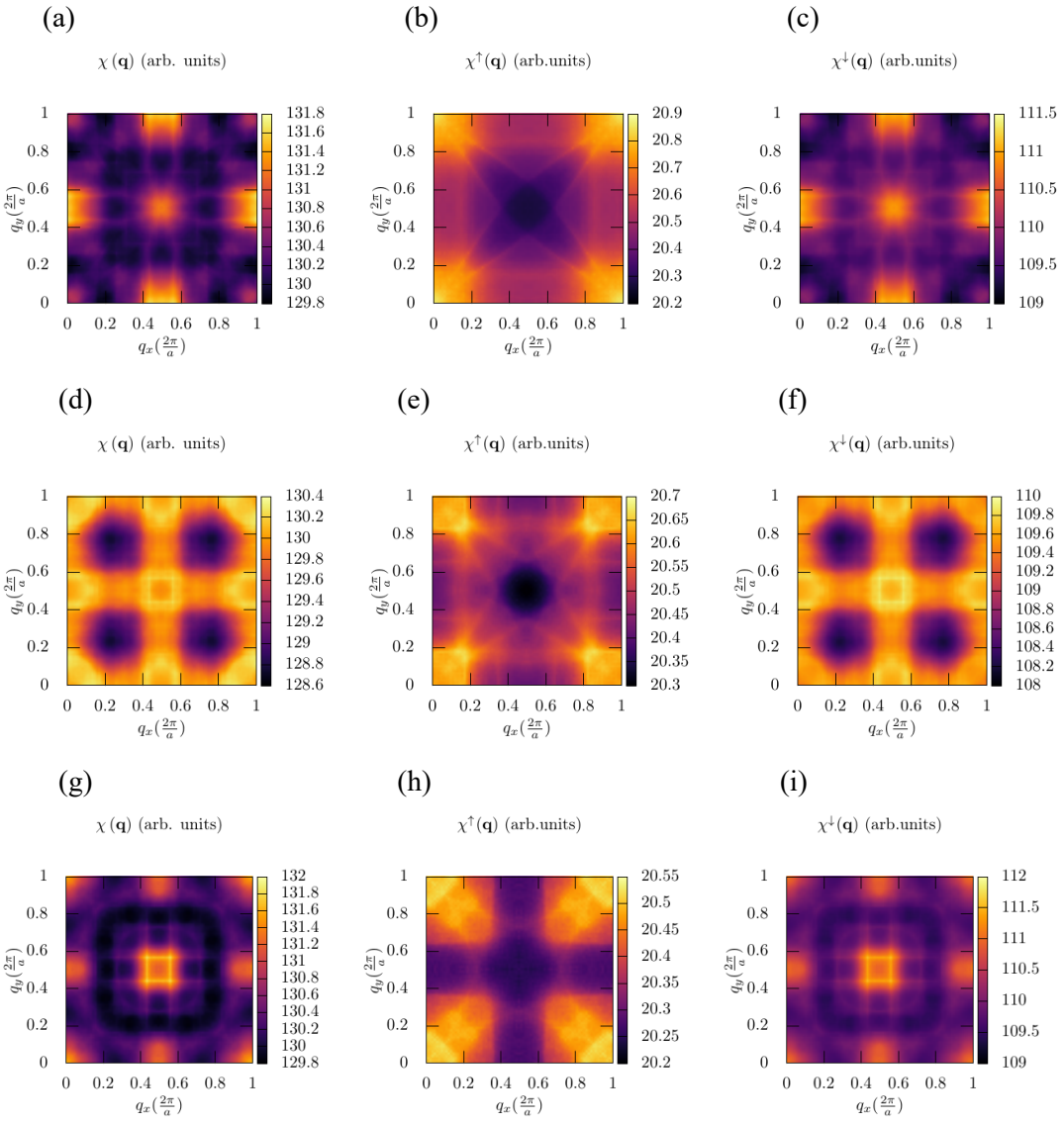

Fig. B1. QSGW generalized susceptibility of the total $\chi(\boldsymbol{q})$, majority-spin $\chi^{\uparrow}(\boldsymbol{q})$, and minority-spin $\chi^{\downarrow}(\boldsymbol{q})$ components in Fe_3Pd with (a)-(c) with $q_z = 0$; (d)-(f) with $q_z = \left(\frac{2\pi}{a}\right) \times \frac{1}{4}$; (g)-(i) with $q_z = \left(\frac{2\pi}{a}\right) \times \frac{1}{2}$.

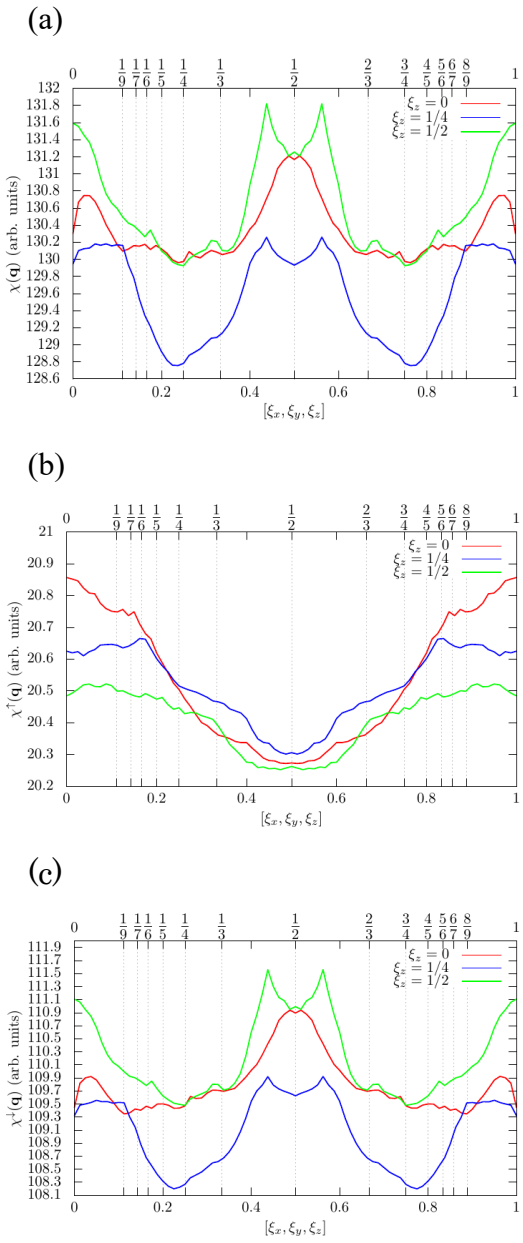

Fig. B2. Profile of the QSGW generalized susceptibility along the $[1, 1, 0]$ direction in Fe_3Pd: (a) total $\chi(\boldsymbol{q})$, (b) majority-spin $\chi^{\uparrow}(\boldsymbol{q})$, and (c) minority-spin $\chi^{\downarrow}(\boldsymbol{q})$ components at $[\xi_x, \xi_y, \xi_z]$.

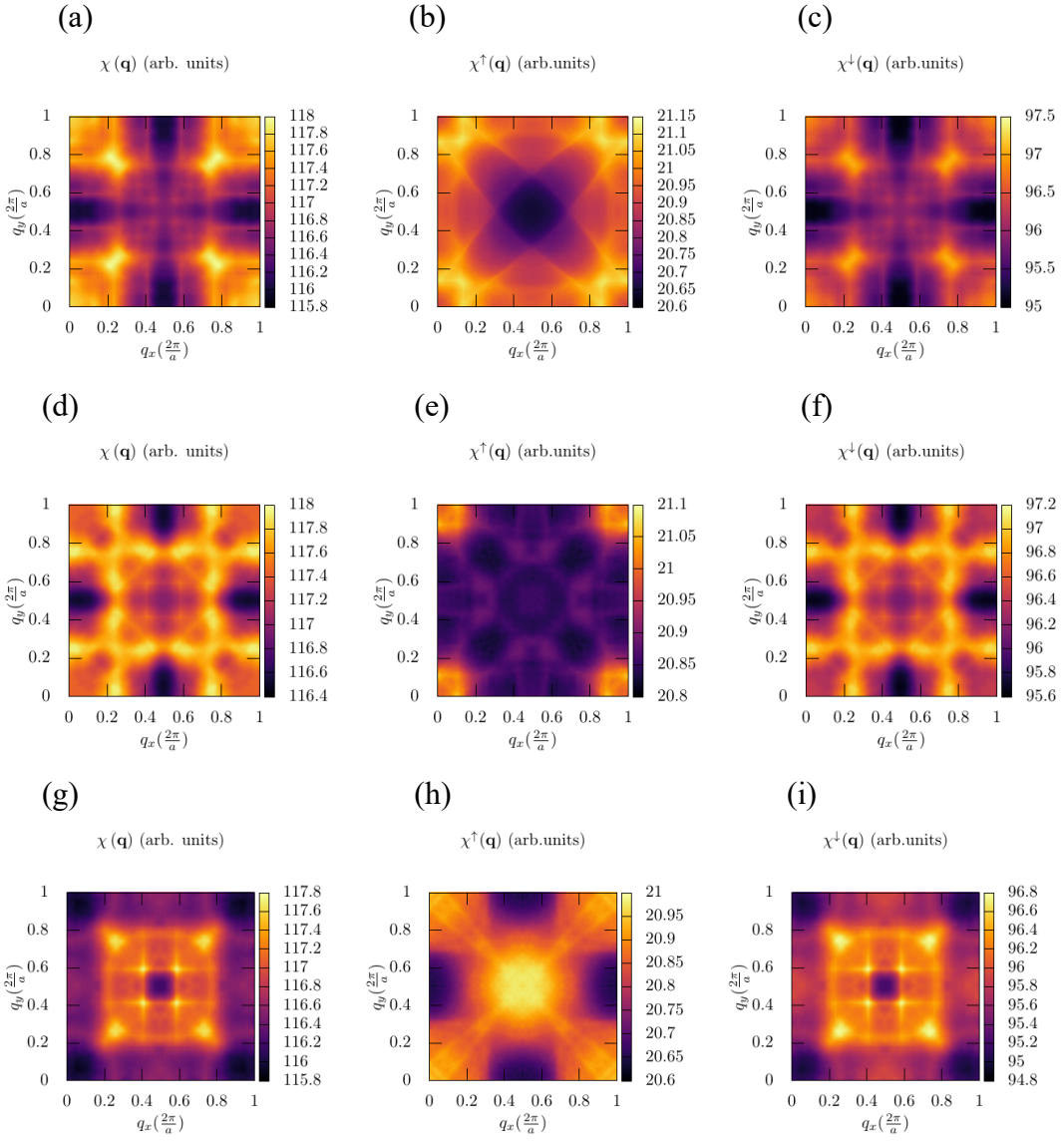

Fig. B3. QSGW generalized susceptibility of the total $\chi(\boldsymbol{q})$, majority-spin $\chi^{\uparrow}(\boldsymbol{q})$, and minority-spin $\chi^{\downarrow}(\boldsymbol{q})$ components in Fe_3Pt with (a)-(c) with $q_z = 0$; (d)-(f) with $q_z = \left(\frac{2\pi}{a}\right) \times \frac{1}{4}$; (g)-(i) with $q_z = \left(\frac{2\pi}{a}\right) \times \frac{1}{2}$.

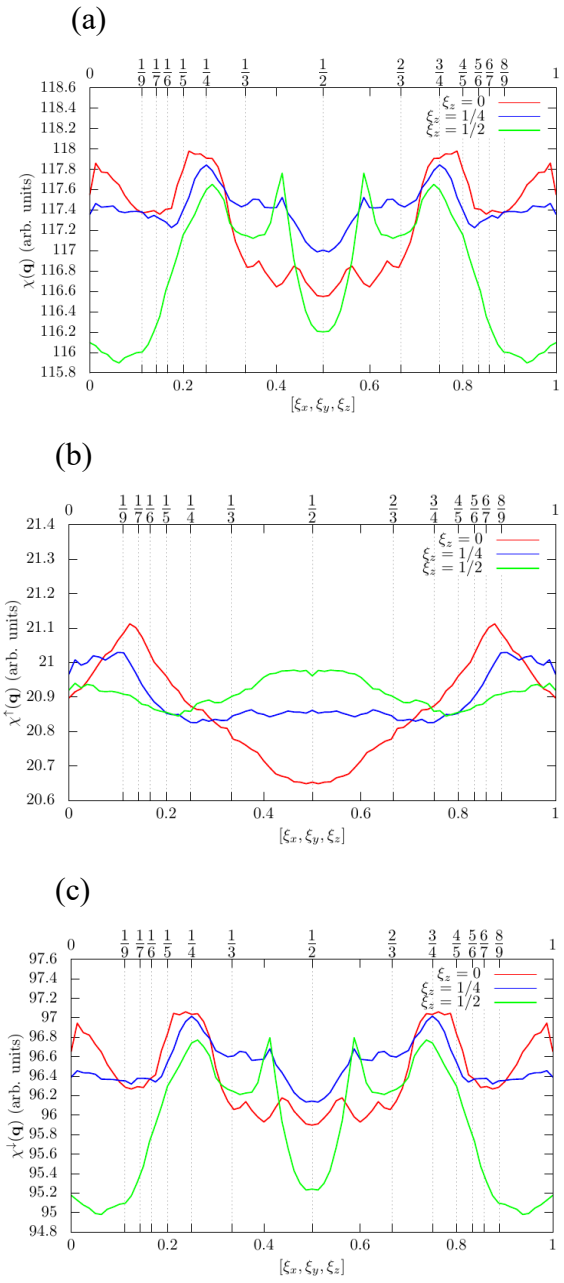

Fig. B4. Profile of the QSGW generalized susceptibility along the $[1, 1, 0]$ direction in Fe_3Pt: (a) total $\chi(\boldsymbol{q})$, (b) majority-spin $\chi^{\uparrow}(\boldsymbol{q})$, and (c) minority-spin $\chi^{\downarrow}(\boldsymbol{q})$ components at $[\xi_x, \xi_y, \xi_z]$.

Appendix C

Figures C1 presents the contour maps of generalized susceptibility $\chi(\boldsymbol{q})$ for the SOI version without Fermi energy shift ($\Delta E_{\mathrm{F}} = 0$) in Fe_3Pt. In the evaluation, all of the eigenvalues combined with both spin states were used. Therefore, the resulting values are larger in Fig. C1 and it is not possible to separate the majority- and minority-spin components. The peaks for the susceptibility $\chi(\boldsymbol{q})$ exhibit broadening compared to without SOI. The resulting profile implies large values near $[\xi, 0, 0]$ with the $\xi = 1/2$ and $[\xi, \xi, \xi]$ with the $\xi = 1/4$. Since these peaks are broad, further studies are needed to determine a definitive conclusion on the property of electronic instability.

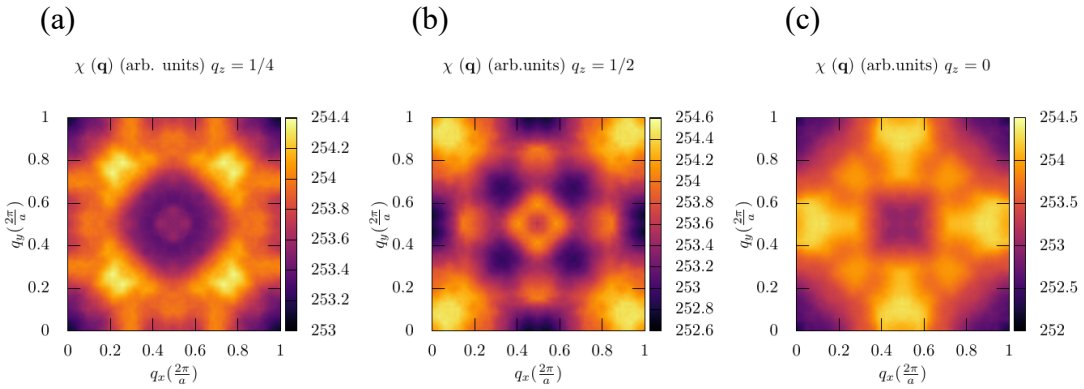

Fig. C1. QSGW Generalized susceptibility of the total $\chi(\boldsymbol{q})$ with SOI in Fe_3Pt with (a) $q_z = \left(\frac{2\pi}{a}\right) \times \frac{1}{4}$; (b) $q_z = \left(\frac{2\pi}{a}\right) \times \frac{1}{2}$; (c) $q_z = 0$.